AGU PUBLICATIONS

JGR

Journal of Geophysical Research: Oceans

RESEARCH ARTICLE

10.1002/2014JC010187

Key Points:
- We identify the mechanisms controlling fine deposits
- Numerical model output was compared with bottom sediment observations
- Characterization the multiple spatial and temporal scales involved

Correspondence to:
M. Grifoll,
manel.grifoll@upc.edu

Citation:
Grifoll, M., V. Gracia, A. Aretxabaleta, J. Guillén, M. Espino, and J. C. Warner (2014), Formation of fine sediment deposit from a flash flood river in the Mediterranean Sea, *J. Geophys. Res. Oceans*, *119*, 5837–5853, doi:10.1002/2014JC010187.

Received 28 MAY 2014
Accepted 11 AUG 2014
Accepted article online 14 AUG 2014
Published online 9 SEP 2014

Formation of fine sediment deposit from a flash flood river in the Mediterranean Sea

Manel Grifoll[1,2], Vicenç Gracia[1,2], Alfredo Aretxabaleta[3], Jorge Guillén[4], Manuel Espino[1,2], and John C. Warner[3]

[1]Laboratori d'Enginyeria Marítima, Universitat Politècnica de Catalunya, Barcelona, Spain, [2]Centre Internacional d'Investigació dels Recursos Costaners, Barcelona, Spain, [3]U.S. Geological Survey, Woods Hole, Massachusetts, USA, [4]Institut de Ciencies del Mar, CSIC, Barcelona, Spain

Abstract We identify the mechanisms controlling fine deposits on the inner-shelf in front of the Besòs River, in the northwestern Mediterranean Sea. This river is characterized by a flash flood regime discharging large amounts of water (more than 20 times the mean water discharge) and sediment in very short periods lasting from hours to few days. Numerical model output was compared with bottom sediment observations and used to characterize the multiple spatial and temporal scales involved in offshore sediment deposit formation. A high-resolution (50 m grid size) coupled hydrodynamic-wave-sediment transport model was applied to the initial stages of the sediment dispersal after a storm-related flood event. After the flood, sediment accumulation was predominantly confined to an area near the coastline as a result of preferential deposition during the final stage of the storm. Subsequent reworking occurred due to wave-induced bottom shear stress that resuspended fine materials, with seaward flow exporting them toward the midshelf. Wave characteristics, sediment availability, and shelf circulation determined the transport after the reworking and the final sediment deposition location. One year simulations of the regional area revealed a prevalent southwestward average flow with increased intensity downstream. The circulation pattern was consistent with the observed fine deposit depocenter being shifted southward from the river mouth. At the southern edge, bathymetry controlled the fine deposition by inducing near-bottom flow convergence enhancing bottom shear stress. According to the short-term and long-term analyses, a seasonal pattern in the fine deposit formation is expected.

1. Introduction

River sediment deposition and dispersal over the continental shelf depend on oceanographic conditions, river sediment character and load, and shelf morphological characteristics [*McCave*, 1972; *Wright and Nittrouer*, 1995; *Díaz et al*., 1996; *George and Hill*, 2008]. Fine deposits or mud belts are formed by prograding sequences of accumulation of fine sediment over the continental shelf. A quantitative understanding of the transport of material from rivers during single episodes may resolve time scales associated with stratigraphic processes [*Harris et al*., 2008; *Warner et al*., 2008a].

The river-borne sediment dispersal and the interface between the river and the shelf involve physical and geological mechanisms acting at different temporal and spatial scales [*Wright and Nittrouer*, 1995]. Observational studies have revealed that, in many coastal environments, episodic storms dominate the sediment fluxes and the subsequent dispersal patterns [*Sherwood et al*., 1994; *Ogston and Sternberg*, 1999; *Guillén et al*., 2006; *Bourrin et al*., 2008; *Warner et al*., 2008a; *Bever et al*., 2011; *Grifoll et al*., 2013a]. The sediment flux during storm events can be several orders of magnitude larger than during calm conditions [*Guillén et al*., 2006; *Ulses et al*., 2008; *Bever et al*., 2011]. In consequence, preferential depositional patterns during river floods can partially explain long-term fine deposits observed on the seafloor [*Ogston et al*., 2000; *Fan et al*., 2004]. On longer time scales, advection of sediment by shelf currents can redistribute sediment and determine final deposition patterns [*Sherwood et al*., 1994; *Ogston et al*., 2000; *Harris et al*., 2008; *Bever et al*., 2009; *Xu et al*., 2011; *Xue et al*., 2012]. Granulometric parameters are often the best indicators of net across-shelf transport integrated in long-time scales [*Nittrouer and Wright*, 1994].

Recently, sediment dynamics on continental shelves have been investigated using advanced modeling tools. *Warner et al*. [2008a] used a numerical system to analyze storm-driven sediment transport in

Massachusetts Bay and compared numerical results with observed bottom sediment grain size. *Harris et al*. [2008] studied sediment concentration advected by shelf currents and its subsequent large-scale deposition in the northwestern Adriatic Sea. *Xu et al*. [2011] analyzed the dispersal of sediment over the Texas-Louisiana shelf assessing fluvial sediment accumulation. *Bever and Harris* [2013] studied the sediment transport from Waipaoa River in Poverty Bay (New Zealand) describing sediment transit and export to the continental shelf. These examples used a coupled wave, current, and sediment transport model to simulate the interactions of waves and currents in the bottom boundary layer and the associated sediment resuspension/settling.

The northwest (NW) Mediterranean basin contains short rivers that exhibit brief and sudden freshwater discharge (lasting from hours to a few days) named flash floods. These energetic episodes are mainly associated with low-pressure atmospheric systems during spring and fall. The result of the freshwater discharge is the sudden transport of sediment to the coastal zone. Sediment dispersal from these flash flood rivers remains poorly understood. An observational study of the sedimentary dynamics of a flash flood river in the NW Mediterranean Sea (Tet River) *Guillén et al*. [2006] concluded that sediment distribution on the shelf followed a complex, multistep pattern as a result of the influence of multiple events. In their study, an initial deposition of an ephemeral layer during a "wet" storm (high rainfall rates) was followed by resuspension and exporting of sediment to the midshelf. The final location of the fine sediment deposit was unclear (limited by the length and breadth of their observations) and only partially transported by offshore flow.

We investigate the driving mechanisms that govern the distribution of an observed fine deposit (or mud belt) in front of the Besòs River in the NW Mediterranean Sea. Due to the different scales involved in the sedimentary process, various simulations have been designed to investigate different temporal and spatial scales. First, we introduce the basic characteristics of the fine deposit in the study area and the modeling system and scenarios (section 2). We focus on two simulations: (1) a high-resolution local simulation of a flash flood event and subsequent reworking during 11–20 March 2011; and (2) a 1 year simulation from May 2010 to April 2011 at a regional scale. Section 3 includes the results of the numerical simulations and field data highlighting the fine sediment deposit thickness and the hydrodynamic variables that explain sediment accumulation. The results, the sensitivity to sediment parameters, and the comparison with other areas are examined in section 4.

2. Location, Data, and Methods

2.1. Study Area

The Besòs River, with a length of 51.6 km, is a small mountainous river in Spain that has characteristics of a flash flood regime. The catchment area is relatively small (1028.9 km^2). The mean water discharge is 6.8 $m^3 \cdot s^{-1}$, although during flash flood events can reach more than 20 times this magnitude. *Liquete et al*. [2009] estimated an annual sediment discharge of 16×10^3 $t \cdot yr^{-1}$ based on observations. These authors also reported a high variability of the instantaneous river sediment load as expected in a flash flood regime.

A narrow and relatively steep shelf (15 km wide) characterizes the geomorphology of the area offshore of the mouth of the Besòs River. North of the mouth, the shelf is wider than to the south in front of Barcelona Harbor (Figure 1). The regional oceanographic conditions are characterized by a microtidal regime while the wave regime is fetch-limited. The shelf flow in front of the Besòs mouth has been characterized from observations and numerical simulations [*Grifoll et al*., 2012, 2013b]. Water current observations at 24 and 50 m revealed along-shelf polarization of the flow. The along-shelf fluctuations respond to local wind stress in short-time scales and remote pressure gradients in synoptic time scales. Two field campaigns (November 2010 to January 2011 and March–April 2011) measured oceanographic (waves, currents, and suspended sediment concentration near bottom), atmospheric (wind intensity and direction), and river (discharge flow) variables (see details in *Grifoll et al*. [2012, 2013a]). During the measurements, a flash flood event was captured during 11–16 March 2011. These data sets were used to assess the skill of the numerical model flows.

The wave climate in the region is controlled by a heterogeneous wind field with E, NW, and S being the predominant components [*Bolaños et al*., 2009]. The incident waves in front of the Besòs River come predominantly from two directions: E-NE and S-SW [*Alomar et al*., 2014]. Even with the relatively short fetch, typical annual storms can generate offshore significant wave heights up to 5 m with associated peak periods of up to 13 s. The most energetic storms occur during fall and winter. During spring and summer, the wave

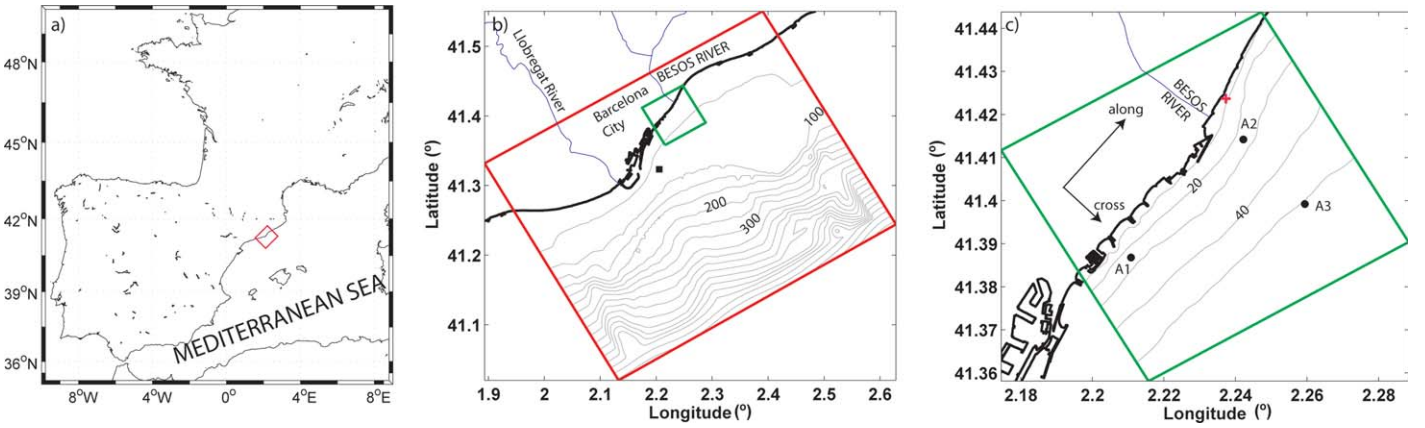

Figure 1. (a) Location of the study area in the NW Mediterranean Sea. (b, c) Bathymetry and model boundaries of the COASTAL (in red) and LOCAL (in green) meshes. The square in Figure 1b shows the position of the wave buoy used to obtain the wave boundary conditions for the LOCAL simulation. The circles in Figure 1c show the current meter profiles mounted during the field campaigns (i.e., A1, A2, and A3). The red cross in Figure 1c shows the Coastal Observatory Station where wind parameters were recorded. The axis system used for the hydrodynamic and sediment fluxes (i.e., cross- and along-shelf directions) is shown in Figure 1c.

conditions are less energetic. Waves approaching from the east represent the most frequent direction with typical storm duration of 24 h.

Previous studies of sedimentary processes in the region [*Jiménez et al*., 1999; *Puig et al*., 2001; *Palanques et al*., 2002; *Ferré et al*., 2005; *Guillén et al*., 2006; *Grifoll et al*., 2013a] agreed that waves are the main resuspension mechanisms in the inner/midshelf in the NW Mediterranean Sea with prevalent along-shelf fluxes. Using the data from the March–April 2011 field campaign, *Grifoll et al*. [2013a] found that the suspended sediment concentrations were correlated with river flow discharge and energetic wave events. This differs from other shelves with strong tides and long-period waves where resuspension by waves during extreme events can reach the outer shelf [*Sherwood et al*., 1994] and cross-shelf and along-shelf fluxes might be of the same order of magnitude [*Palanques et al*., 2002].

The spatial extent of the mud deposits was obtained from a compilation of historical sediment grain-size observations (Figure 2). The mud fraction has been considered as sediment quartz-equivalent diameter less than 63 μm [*McCave*, 1972] or $\emptyset > 4$. Larger grain sizes were observed in the shallower boundary forming a sand/mud transition with coarse sand in the vicinity of the Barcelona city sandy beaches. The mud belt extends from the river mouth toward the southwest for several kilometers, and also from the river mouth to the north but with a lesser northeast extension. *Liquete et al*. [2007] used seismic reflection profiles to define the fine sediments in the continental shelf off Barcelona. From these data, the main sedimentary body presents an elongated area of about 5 × 2 km and is located approximately between the 30 and 65 m isobaths. From the seismic results, a qualitative correlation between grain size and backscatter values from seismic data suggests the midshelf depocenter is shifted southeast of the Besòs River mouth.

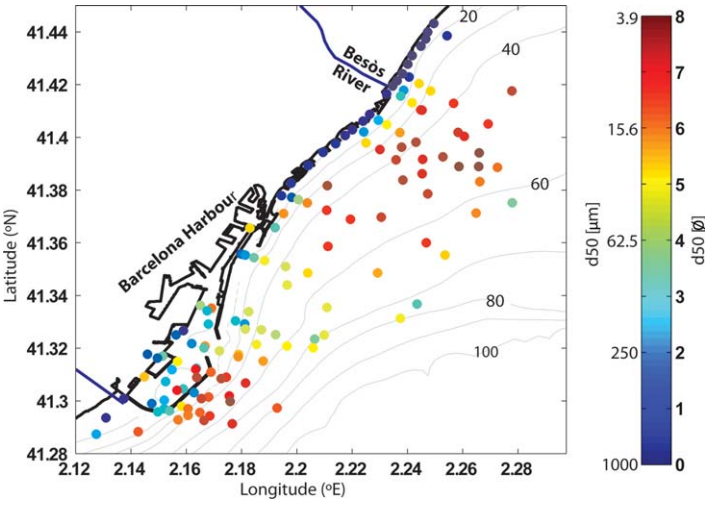

Figure 2. Compilation of historical observations of sediment texture. Grain size expressed in μm and ø: $\text{ø} = -\log_2(D_{50})$, where D_{50} is the particle size in mm. The bathymetry is also included in gray. The deepest isobath plotted is 100 m, which represents the shelf break.

Table 1. Sediment Classes and Hydrodynamics Properties Used in the Numerical Model for the Besòs River Sediment Load

Class	Diameter (μm)	W_s (mm·s^{-1})	T_{cr} (N·m^{-2})	E (Kg·m^{-2}·s^{-1})	Percentage of Rating in Sediment Suspended Discharge (%)
1	7.8	0.038	0.05	5×10^{-4}	50
2	15	0.15	0.05	5×10^{-4}	50

2.2. Modeling System and Scenarios

The Coupled Ocean-Atmosphere-Wave-Sediment Transport modeling system (COAWST) [*Warner et al*., 2010] was chosen to model the hydrodynamic conditions and the transport and dispersal of sediment from the Besòs River. The COAWST system consists of several state-of-the-art models that include ROMS (Regional Ocean Modeling System) [*Shchepetkin and McWilliams*, 2005] for ocean circulation and SWAN (Simulating Waves Nearshore) [*Booij et al*., 1999] for surface wind wave. The system includes the CSTMS (Community Sediment Transport Modeling System) [*Warner et al*., 2008b] sediment transport module embedded in ROMS. The wave model provides hydrodynamic parameters (i.e., significant wave height, average wave periods, wave propagation direction, near-bottom orbital velocity, and wave energy dissipation rate) to the water circulation model. The ocean model provides water depth, sea surface elevation, and current velocity to the wave model. The sediment module CSTMS allows the definition of multiple sediment classes and evaluates bed and suspended sediment transport including sediment settling, resuspension by waves and currents, and sediment advection by currents. An active bed layer controls the depth available for resuspension whose thickness varies according to bottom shear stress. Deposition was calculated from the bottom boundary condition of the settling flux algorithm. The erosive and depositional fluxes were added at each time step to obtain net mass transfers to the bottom cell in the water column [*Warner et al*., 2008b].

Two nested domains were used in the simulations: the COASTAL and LOCAL meshes (Figure 1). The COASTAL mesh had 250 m horizontal resolution and encompassed the shelf from the coast until the shelf break and upper slope. Embedded in the COASTAL mesh, a LOCAL mesh of 50 m horizontal resolution covered the vicinity of the Besòs mouth. Such nesting strategy was chosen to capture the different temporal and spatial scales. The simulations conducted in both meshes employed two-way SWAN-ROMS coupling. The wave effect on currents was considered in an Eulerian-averaged reference frame expressed as a Vortex Force [*Kumar et al*., 2012]. The vertical water-column resolution of both domains had 20 sigma layers, which resolved both surface and bottom boundary layers. A generic length scale turbulent mixing scheme [*Umlauf and Burchard*, 2003] implemented within ROMS by *Warner et al*. [2005] was used in both COASTAL and LOCAL simulations with coefficients selected to parameterize the κ-ε scheme [*Rodi*, 1987]. The implementation included fourth-order biharmonic Laplacian viscosity and mixing terms in geopotential surfaces for velocity and tracers, respectively, both with constant coefficients of 0.5 m^4 s^{-2}. For both COASTAL and LOCAL simulations, the bottom boundary layer was parameterized using the combined wave-current Madsen model [*Madsen*, 1994]. A uniform value of 0.005 m was used for the bottom roughness by the Madsen model assuming a certain level of error in the bottom stress [*Madsen et al*., 1993; *Dalyander et al*., 2013]. This value leads to reasonable agreement between the model results and the observations in terms of bottom current [*Grifoll et al*., 2013b].

The wave conditions at the open boundary of the COASTAL model were provided by measurements of a directional buoy moored at 68 m (managed by the Spanish Harbour Agency, www.puertos.es; Figure 1). The wave conditions for the LOCAL simulation were extracted from the COASTAL solution. The oceanographic conditions (velocity, temperature, salinity, sea level) at the open boundaries were obtained from a regional model simulation [*Grifoll et al*., 2013b] that covered the Catalan shelf nested into the MyOcean oceanic model [*Tonani et al*., 2009]. The atmospheric heat flux and wind were provided by ECMWF in the regional simulations (COASTAL domain) [*Grifoll et al*. [2013b], while we used observational winds measured at the Coastal Observatory Station (location in Figure 1c) for the local simulations (LOCAL domain).

The LOCAL simulation included the sediment transport module and was used to characterize the period 10–21 March 2011, which included a flash flood event (11–16 March 2011), a calm period, and an energetic wave period lasting 1 day (20 March). Two fine sediment classes (diameters of 7.8 and 15 μm) were used to represent the suspended sediment discharge [*Bever et al*., 2009; *Bever and Harris*, 2013] and the observed fine deposit (Table 1). The model was initialized with no sediment in the system being the only source as the riverine sediment classes. The settling velocities (W_s) were set according to *Fox et al*. [2004]. The critical

shear stress (τ_{cr}) was set to 0.05 Pa. This value was larger than Shield's critical stress to consider the multiple physical and biological factors that influence cohesion strength [*Van Ledden et al.*, 2004]. This value is also representative based on the initiation of resuspension observed at A1 and A2 [*Grifoll et al.*, 2013a] as a function of the combined bottom stress estimated from observations. The surface erosion mass is computed linearly through the excess of shear stress (wave-current bottom shear stress minus critical stress: $\tau_{wc}-\tau_{cr}$). The erosion flux has been evaluated as in *Ariathurai and Arulanandan* [1978]:

$$E=E_0\cdot(1-\theta)\cdot\frac{\tau_{wc}-\tau_{cr}}{\tau_{cr}}, \quad (1)$$

where E_0 is the sediment erodibility constant (kg m^{-2} s^{-1}) and θ is porosity. For the numerical calculations the sediment density was 2650 kg·m^{-3} and the porosity 0.6 [*Bever et al.*, 2009]. Erosion rate can vary several orders of magnitude [*Amoudry and Souza*, 2011], so a tentative value was chosen (5×10^{-3} kg·m^{-2}·s^{-1}) and a sensitivity test is discussed in section 4.1. The river suspended sediment yield in the Besòs River does not follow the log-relation with flow of the typical sediment-rating curve [*Liquete et al.*, 2009]. Rating curves for a similar river (Tordera River with a catchment area adjacent and similar to the Besòs River) were obtained observationally providing suspended sediment concentration of the order of a few g·L^{-1} during floods [*Rovira and Batalla*, 2006]. No suspended sediment yield was measured during the LOCAL simulation period so a river suspended sediment concentration of 1 g·L^{-1} was chosen. This value is similar to the sediment concentration observed in the Tet River [*Guillén et al.*, 2006]. The Tet, located 160 km north of Besòs River, also experiences a flash flood regime with a mean flow of similar magnitude to the Besòs River (10 m^3·s^{-1} in the Tet versus 6.9 m^3·s^{-1} in the Besòs River). The mass, temperature, and salinity fluxes were included in two contiguous cells as point sources.

Although sediment pulses are capable of depositing sediment on the shelf, the final depositional configuration may be controlled by advective processes [*Harris et al.*, 2008; *Bever and Harris*, 2013; *Dufois et al.*, 2014]. The yearlong regional circulation has been analyzed using the COASTAL simulation, which covers a larger spatial extent (Figure 1). A statistical quantification of the combined bottoms stress provided spatial information of the energetic areas on the shelf. Reduced bottom stress areas correspond with regions where finer sediment was expected. The 5% exceedance value (95th percentile) is used as a characterization of the spatial distribution of the largest bottom stresses [*Dalyander et al.*, 2013].

Seabed mobility was assessed at discrete locations where grain-size observations were available. At these locations, modeled wave-current bottom stresses were compared to the grain-size critical stress threshold [*Soulsby*, 1997] using observed sediment texture measurements. The bed mobility was established as the percentage of time the critical stress at each sample location was exceeded [*Dalyander et al.*, 2013]. Two different periods were considered to explore intra-annual variability in bed mobility. One period covered spring and summer, where wave conditions are reduced in magnitude, and the other fall and winter, where energetic events are more common.

3. Results

3.1. Flash Flood Hydrodynamics

The storm during 11–16 March 2011 was characterized by intense precipitation and subsequent increased river flow. Freshwater peak discharge of 170 m^3·s^{-1} was recorded in a flowmeter station mounted near the mouth (Figure 3a; data provided by the Water Catalan Agency; www.gencat.cat/aca) and was more than 20 times higher than mean conditions (6.8 m^3·s^{-1}). North-easterly wind with maximum intensity of 13 m·s^{-1} (13 March) and two energetic peaks of similar magnitude (12 and 14 March; Figure 3b) were measured at the Coastal Observatory Station. After the storm, relatively calm conditions were recorded.

The depth-averaged velocity time series (Figures 3c and 3d) showed flow intensification in the along-shelf direction during 11–16 March caused by enhanced wind intensity [*Grifoll et al.*, 2012]. Depth-averaged velocities reached 30 cm·s^{-1}. The velocity recorded at A1 exhibited strong correlation with velocities at A2 and A3. Cross-shelf velocity magnitudes were smaller than along-shelf flow. The depth-averaged cross-shelf velocities for A2 and A3 showed a prevalent seaward component (Figure 3d).

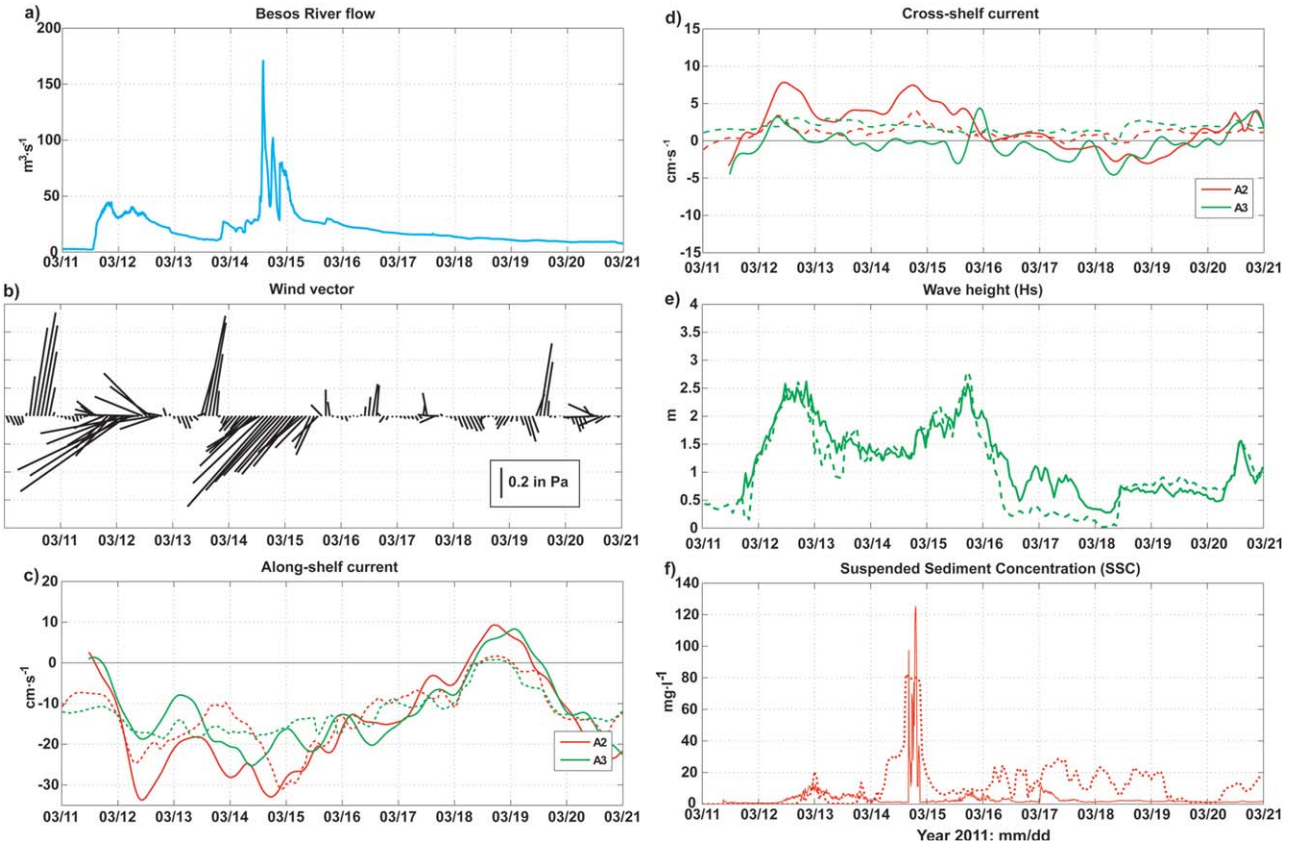

Figure 3. Flash flood (a) Besòs River freshwater discharge; (b) wind stress stick-plot (in Pa); (c) depth-averaged along-shelf velocities (filtered with a cutoff period of 5 h); (d) depth-averaged cross-shelf velocities; (e) significant wave height; (f) suspended sediment concentrations measured and modeled (dashed line). Hydrodynamic parameters measured in front of Besòs River are in solid line (red line for measurements in A2 and green for A3). Dashed line corresponds to model outputs in A2 and A3 (red and green, respectively). The along-shelf and cross-shelf axis directions are shown in Figure 1c.

Wave conditions during the moderate storm exhibited two peaks with wave heights exceeding 2.5 m (Figure 3e). Wave directions for this event were predominantly E-SE and wave peak periods were 9 s. At the end of the storm, the significant wave height decreased until 18 March. Then, an energetic period was observed during 20 March with a peak reaching 1.5 m.

The near-bottom suspended sediment concentrations (SSC) were recorded at A2 (Figure 3f) in front of the Besòs River mouth (A2). In the vicinity of the mouth at 24 m, the SSC increase during the storm was correlated with river discharge. The SSC fluctuations were caused by a combination of freshwater river discharge and wave action modulated by the advective processes [*Grifoll et al.*, 2013a].

Table 2. Model Skill Metrics for the Wave, Current, and SSC Characteristics at Measurements Points During the Storm Period Using the LOCAL Simulation (11–21 March 2011)

Parameter	Location	Correlation Coefficient	Bias	RMSD
Significant wave	A1	0.85	−0.23 m	0.51 m
	A2	0.78	−0.42 m	0.63 m
	A3	0.82	−0.37 m	0.58 m
Along-shelf current	A1	0.72	0.06 $m \cdot s^{-1}$	0.10 $m \cdot s^{-1}$
	A2	0.68	0.07 $m \cdot s^{-1}$	0.09 $m \cdot s^{-1}$
	A3	0.74	0.09 $m \cdot s^{-1}$	0.12 $m \cdot s^{-1}$
Cross-shelf current	A1	0.53	0.03 $m \cdot s^{-1}$	0.03 $m \cdot s^{-1}$
	A2	0.52	−0.02 $m \cdot s^{-1}$	0.04 $m \cdot s^{-1}$
	A3	0.41	0.03 $m \cdot s^{-1}$	0.03 $m \cdot s^{-1}$
SSC	A1	0.72	13 $mg \cdot L^{-1}$	17 $mg \cdot L^{-1}$
	A2	0.68	10 $mg \cdot L^{-1}$	23 $mg \cdot L^{-1}$

The modeled along-shelf and cross-shelf velocities at A2 and A3 (Figures 3c and 3d) reproduced the prevalent along-shelf direction with magnitudes similar to observations. The model skill was acceptable for three ADCP sites (Table 2) and better for the along-shelf direction. Near the shore, strong flow intensities were found due to wave-

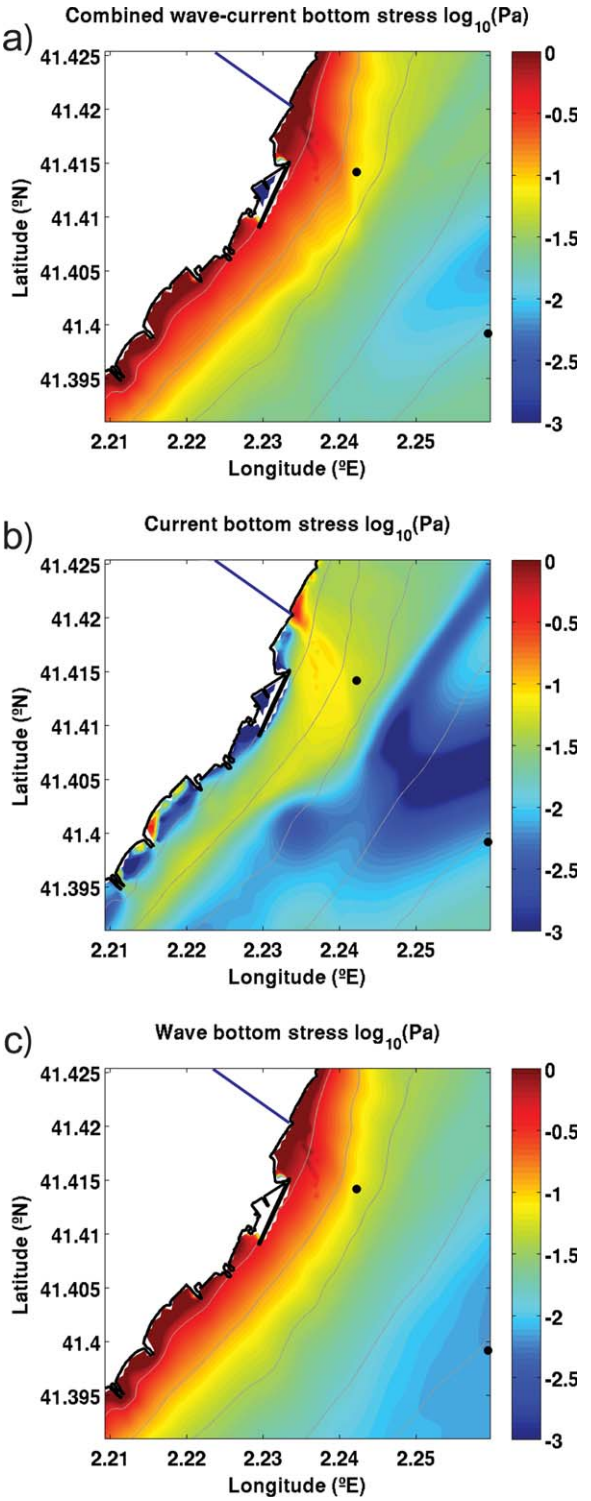

Figure 4. Bed shear stresses $\log_{10}$(Pa) calculated from LOCAL simulation during the flash flood peak. The plot represents a zoom focused in the Besòs River mouth. (a) Combined wave-current component, (b) current stress, and (c) wave stress. Black dots show the ADCP locations. Isobaths are plotted each 10 m.

induced current that prevailed at water depths less than 10 m (not shown).

The modeled significant wave height exhibited good skill (Figure 3e). The model reproduced the timing, duration, and magnitude of the energetic event in most instances. Model bias (Table 2) revealed an underestimation of the wave field possibly caused by smoothed bathymetry and the spatial variability of the wind and wave field. *Pallares et al*. [2014] applied a wave model along the Catalan coast and highlighted the limited accuracy under short-duration and fetch-limited conditions in semienclosed domains. The model also reproduced the E-SE direction observed in the wave measurements (not shown). Model wave height during the river discharge peak was about 2 m.

The combined wave-current bottom shear stress during peak discharge exceeded 2 Pa in the shallow areas of the domain (Figure 4a). The current bottom stress was largest near the river discharge, while the wave-induced stress was largest in a band near the coastline (up to 20 m water depth). In most areas, wave stress was the dominant contributor to the combined wave-current bottom stress (Figures 4b and 4c), except in the proximity of the Besòs River mouth.

3.2. Sediment Deposition and Reworking in the LOCAL Simulation

The sediment deposition pattern for both sediment classes at the end of the storm (18 March; Figures 5a and 5b) exhibited a similar behavior with a preferential depositional area near the coastline and a patchy deposition in the inner-shelf. The deposition pattern at the end of the energetic period (21 March; Figures 5c and 5d) showed that the sediment deposited near the coast at 18 March was eroded and transported seaward.

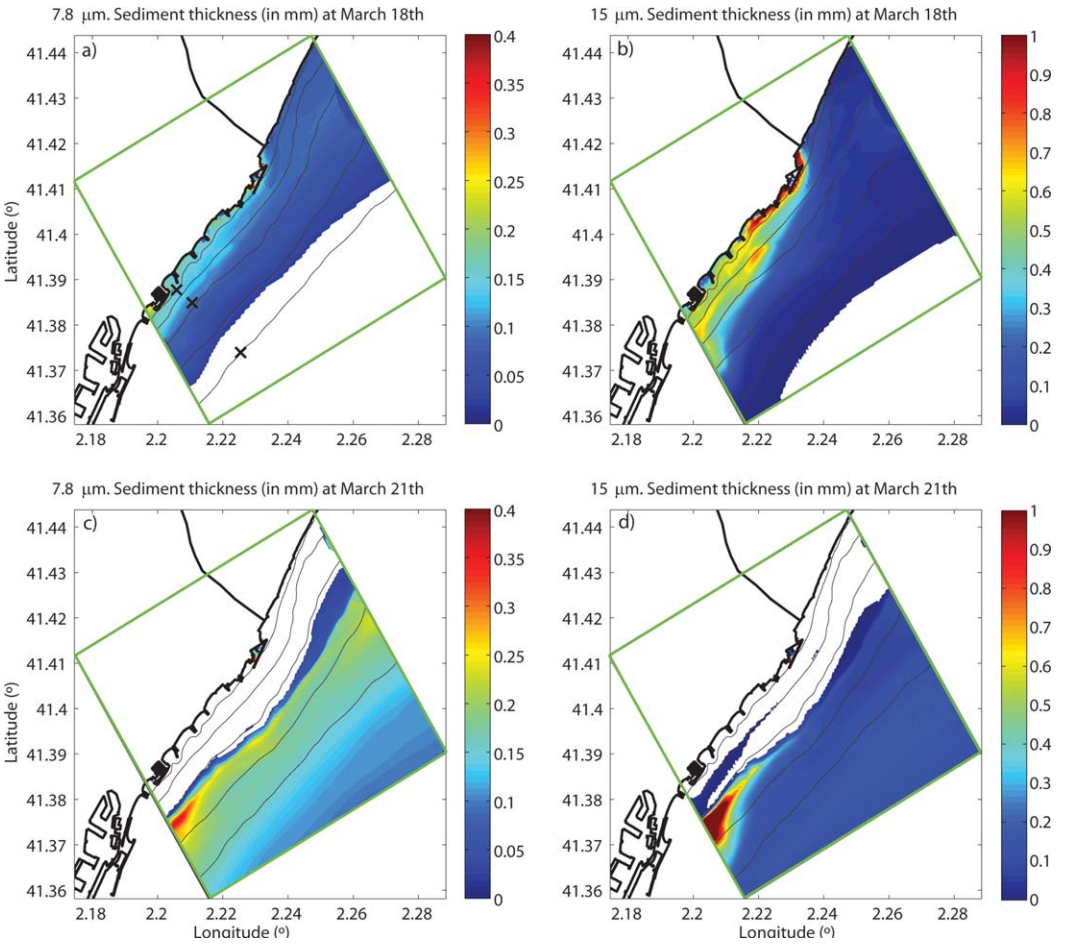

Figure 5. Modeled sediment deposition for (a, b) 18 March at 00:00 and (c, d) 21 March at 00:00 for the LOCAL simulation (the mesh limits are plotted in green) representing both sediment classes: 7.8 and 15 μm. Isobaths are plotted each 10 m. Note that the contour plot varies in ranges. Dark crosses show the control points at 10, 30, and 50 m. When the deposition is zero, the color used is white.

During 21 March, the sediment thicknesses were less than 1 mm with modeled depositional areas located southwestward of the source following the prevalent along-shelf flow (Figure 3c). The coarser material showed larger sediment bed thickness but a smaller depositional area than the finer sediment class.

Hydrodynamic and sedimentary variables from the model outputs were analyzed at three control points covering different bottom depths (10, 30, and 50 m). The control points followed a perpendicular transect southward of Besòs mouth and crossed the modeled mud belt deposits (see control point locations in Figure 5a). The wave conditions at 30 m (Figure 6a) were well correlated with the time series of wave-current bottom shear stress at 10 and 30 m during storm (Figure 6b), which confirms that the combined bottom stress was dominated by wave action.

Large SSC fluctuations at 10 and 30 m were estimated after the river peak discharge occurred (Figures 6c and 6d). SSC was lower at 50 m than at 10 or 30 m bottom depth. Near-bottom along-shelf sediment fluxes (Figures 6e and 6f) were larger than the cross-shelf fluxes (Figures 6g and 6h). The sediment flow was mainly south-westward increasing its magnitude onshore. Near-bottom cross-shelf sediment fluxes exhibited significant seaward pulses. The significant wave height increase during 18 March resulted in an intensification of offshore cross-shelf sediment fluxes at 10 and 30 m for both sediment classes (Figures 6g and 6h). Similar behavior occurred during the significant wave peak of the energetic period (20 March). The bottom stress, SSC, and cross-shelf suspended sediment fluxes time series suggested that the resuspension tends to occur in the shallower zone exporting sediment seaward.

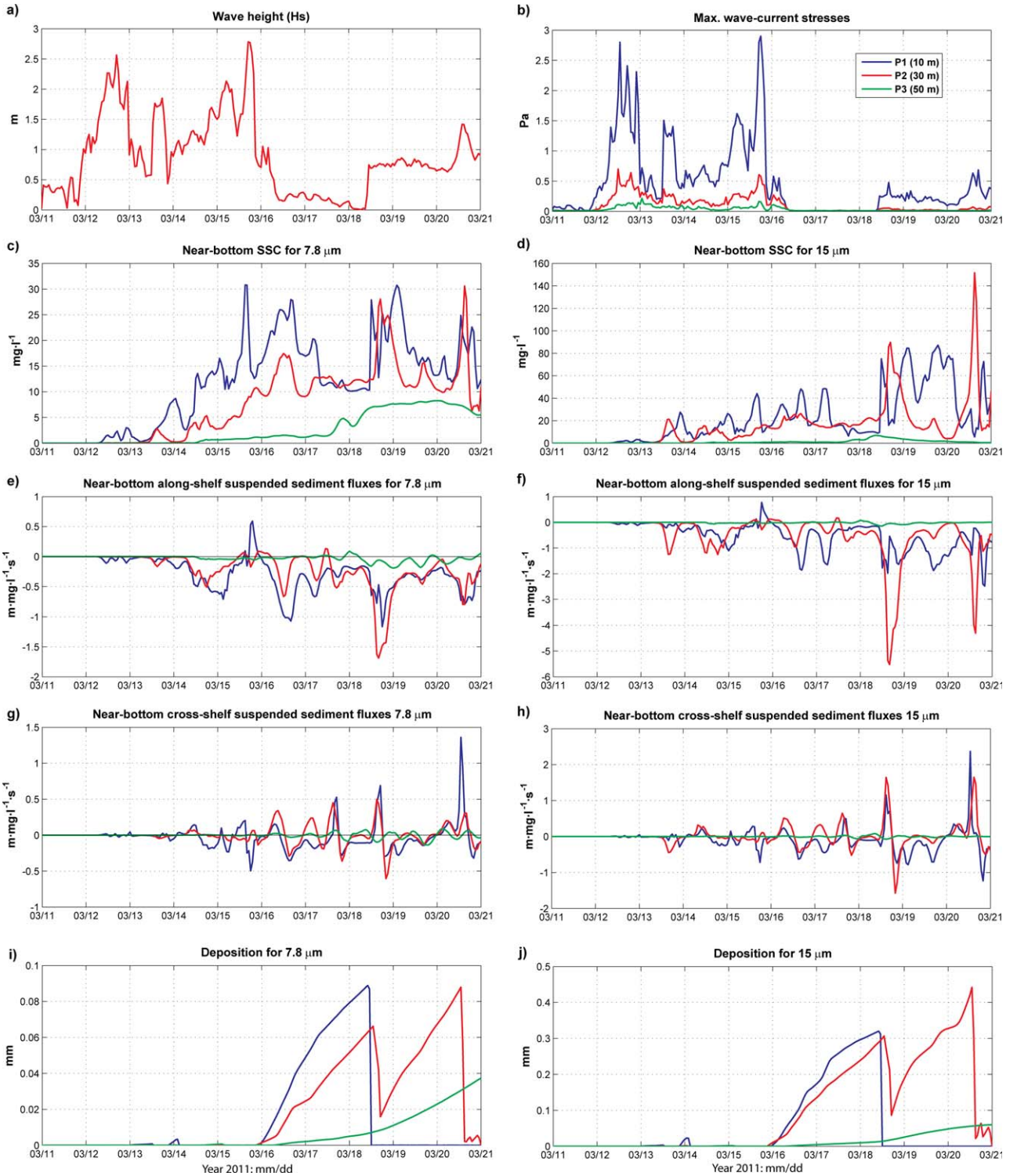

Figure 6. Time series during 11–21 March 2011 at the P1, P2, and P3 control points (see Figure 5a). Left column represents the variables for 7.8 μm sediment class and right column 15 μm sediment class. (a) Significant wave height at P1 (m); (b) combined wave-current bottom stress magnitude (Pa). (c, d) near-bottom Suspended Sediment Concentration (SSC); (e, f) near-bottom along-shelf sediment suspended fluxes; (g, h) near-bottom cross-shelf suspended sediment fluxes; (i, j) deposition thickness. Sediment fluxes are displayed according to the axis directions shown in Figure 1c. Dates in *x* axis represents month/day.

Significant sediment accumulation at 10 and 30 m (control points P1 and P2) began when bottom stress decreased (16 March; Figures 6i and 6j). The deposit thickness at the three control points increased at the end of the storm. When the energetic period started (18 March), the fine deposit was completely eroded at

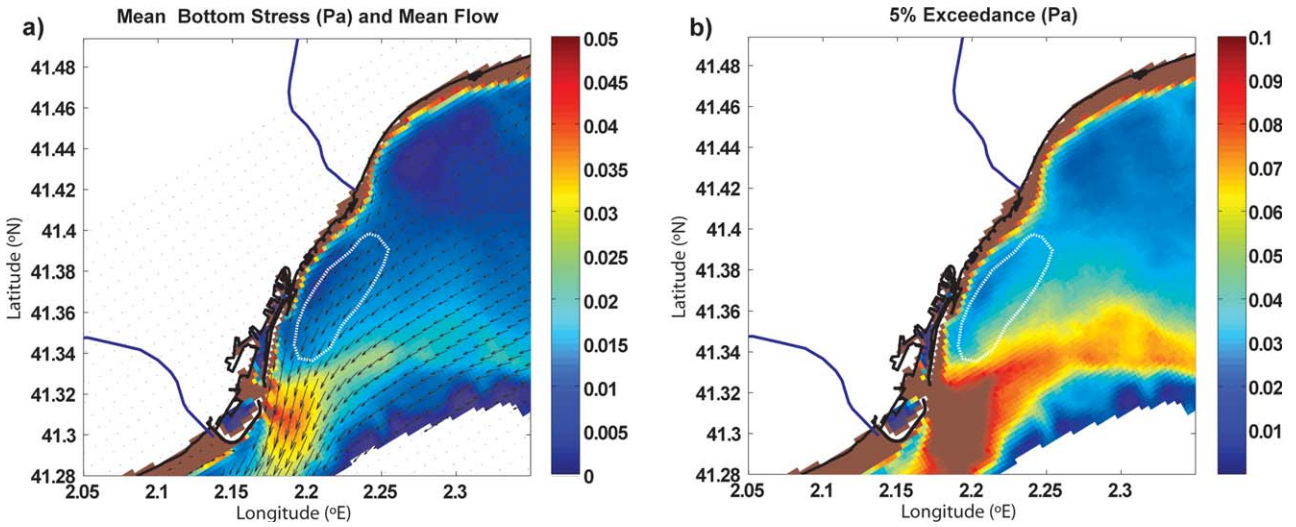

Figure 7. One year results from the COASTAL model. (a) Mean combined bottom stress in (Pa); quiver plot presents the mean depth-averaged flow; (b) 5% of exceedance of combined bottom stresses. The plots only show the results for depths above 150 isobath. The fine grain-size area from seismic data [*Liquete et al.*, 2007] is sketched in white.

10 m bottom depth. At 30 m bottom depth, approximately half of the sediment was eroded, which was consistent with a SSC increase at 30 m water depth. Then, there was no deposition of material at 10 m due to the increase of bottom stress ($\tau > 0.05$ Pa) and the reduction in sediment availability. At 30 m, the bottom stress during 18 March was not able to erode the entire bed thickness and subsequent depositions occurred due to the seaward sediment fluxes (Figures 6g and 6h). After the wave peak of the energetic period (20 March), a complete erosion of deposited sediment was estimated at 30 m increasing SSC. During this period, enhanced bottom stress eroded the previously deposited sediment and increased the seaward sediment fluxes (Figures 6g and 6h).

At 50 m, sediment deposition was characterized by a constant rate uncoupled from the energetic pulses estimated at 10 and 30 m bottom depth. In general, the SSC, sediment fluxes, and deposition rates followed a similar behavior with the finer sediment (7.8 μm) accumulating less than the coarser material. A larger fraction of finer material was exported toward the midshelf or transported south-westward.

3.3. Long-Term (COASTAL) Simulation

The 1 year simulation in the COASTAL domain illustrated the spatial variability of the flow over the shelf. The model results reproduced the along-shelf polarization of the flow (Figure 7a). The 1 year averaged flow was south-westward with intensification in front of Barcelona Harbor. The combined (wave-current) bottom stress was derived from the bottom boundary layer model for the COASTAL mesh. The mean bottom stress was larger when the shelf was narrower and corresponded with areas of maximum velocity in the south edge of Barcelona Harbor (Figure 7a). The flow convergence was caused by a topographic effect that intensified along-shelf flow downstream of the Besòs River. Flow convergence also increased bottom stress along the shelf break. In areas where the bottom current stress was large its standard deviation was of the same order of magnitude than the mean bottom stress suggesting that flow reversals were common (not shown).

The maximum in the 5% exceedance of combined bottom stress occurred at the narrowest part of the shelf ($\tau > 0.05$ Pa) consistent with the intensification of the mean flow offshore of the harbor. The 5% threshold in this region was larger than the critical stress considered for both sediment classes ($T_{cr} = 0.05$ Pa) suggesting the bed was likely composed of sediment coarser than the fine deposit modeled by the LOCAL implementation. This bottom stress distribution was consistent with seabed granulometric observations and seismic data (highlighted in Figure 7) presented by *Liquete et al*. [2007]. The offshore edge of the fine deposit is consistent with the increased bottom stress near the shelf break. In summary, the fine deposits occurred in an area of reduced bottom stress delimited by the numerical results.

Bed mobility was higher during fall-winter than during spring-summer (Figure 8). During fall and winter, bed mobility increased south and north of the Besòs mouth at depths shallower than 30 m. The critical

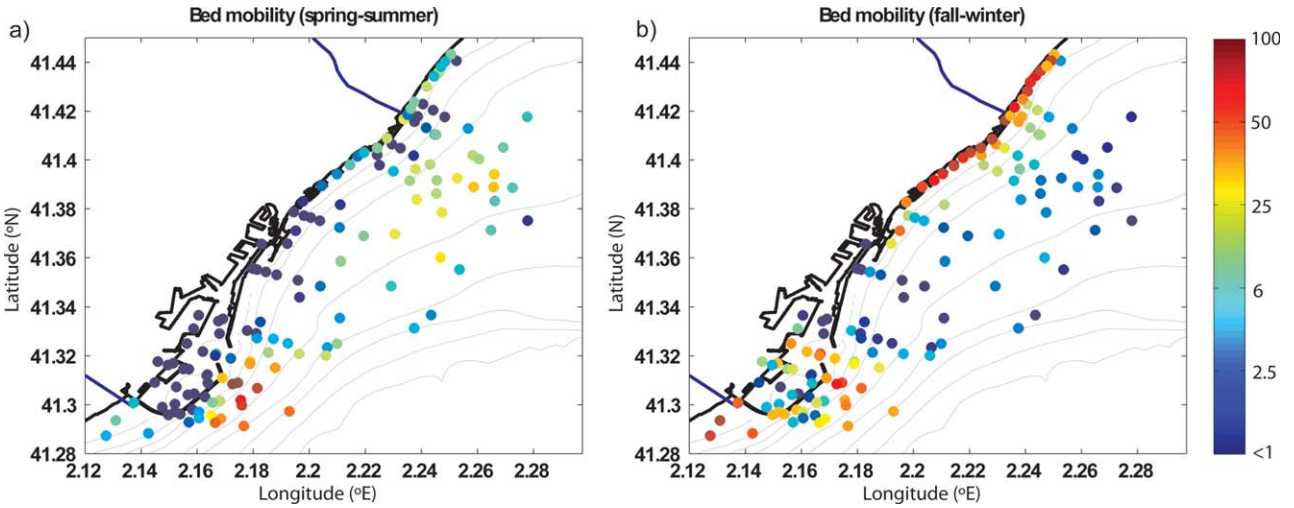

Figure 8. Percentage of time (%) that the critical stress is exceeded (i.e., bed mobility) for the periods (a) spring and summer and (b) fall and winter. The plot scale is transformed in $\log_{10}$.

stress in these areas was exceeded over 40% of the time. Although coarser granulometry was present near the coastline, large bottom stress induced significant bed mobility percentages. Bed mobility over fine deposits exhibited a heterogeneous pattern; during fall-winter the percentage of exceedance remains below 10%, while during spring-summer bed mobility reached 25%. The spring-summer increase was consistent with the prevalent observed south-westward current in the inner-shelf [*Grifoll et al.*, 2013b]. In the south margin of Barcelona, the bed mobility increased due to flow convergence. Although in this area the grain size is larger than the fine deposits, the increased combined bottom stress led to relatively larger mobility.

4. Discussion

4.1. Sediment Accumulation Sensitivity Test

Additional factors that might influence the sediment resuspension during the storm events are bioturbation [*Widdows et al.*, 2009], consolidation [*Dickhudt et al.*, 2011], and trawling [*Palanques et al.*, 2014]. In addition, sediment transport modeling relies on a high degree of empiricism [*Amoudry and Souza*, 2011] and the computations are sensitive to sediment parameter choice [*Xu et al.*, 2011]. As in situ measurements of settling velocities, erosion rate, and river sediment load during the period of analysis were unavailable, we explored the sensitivity to these parameters by considering alternative model scenarios. The comparison between the two sediment classes illustrated the sensitivity to settling velocities. For the smaller sediment grain size (class 2), settling velocities decreased and dispersal of the river sediment increased (Figure 5). Sediment thickness for the larger grain size showed larger accumulation than the finer class. Thus, transport of sediment offshore was more effective for the smaller grain-size fraction, consistent with the grain-size observations.

Additional simulations were conducted using different erosion rates. We used $E_0 = 5 \times 10^{-3}$ kg·m^{-2}·s^{-1} for the reference experiment, but a high variability of this parameter has been found in different environments [*Warner et al.*, 2008a, 2008b; *Bever et al.*, 2009; *Vousdoukas et al.*, 2011; *Bever and Harris*, 2013]. Three additional simulations were conducted testing $E_0 = 5 \times 10^{-4}$ kg·m^{-2}·s^{-1}, $E_0 = 5 \times 10^{-5}$ kg·m^{-2}·s^{-1}, and $E_0 = 5 \times 10^{-6}$ kg·m^{-2}·s^{-1}. The accumulation thickness of the 15 μm class at 10 m bottom depth (Figure 9) was consistent with equation (1); when the erosion rate decreased the erosion fluxes also decreased. The energetic event of 18 March eroded the entire previously deposited sediment bed for the cases 5×10^{-3} and 5×10^{-4} kg·m^{-2}·s^{-1}. In contrast, the experiment with $E_0 = 5 \times 10^{-5}$ kg·m^{-2}·s^{-1} represented a rate-limited case with a larger fraction of deposited sediment and full resuspension not occurring until 21 March. In the case of $E_0 = 5 \times 10^{-6}$ kg·m^{-2}·s^{-1}, no erosion was estimated after 18 March and deposition was

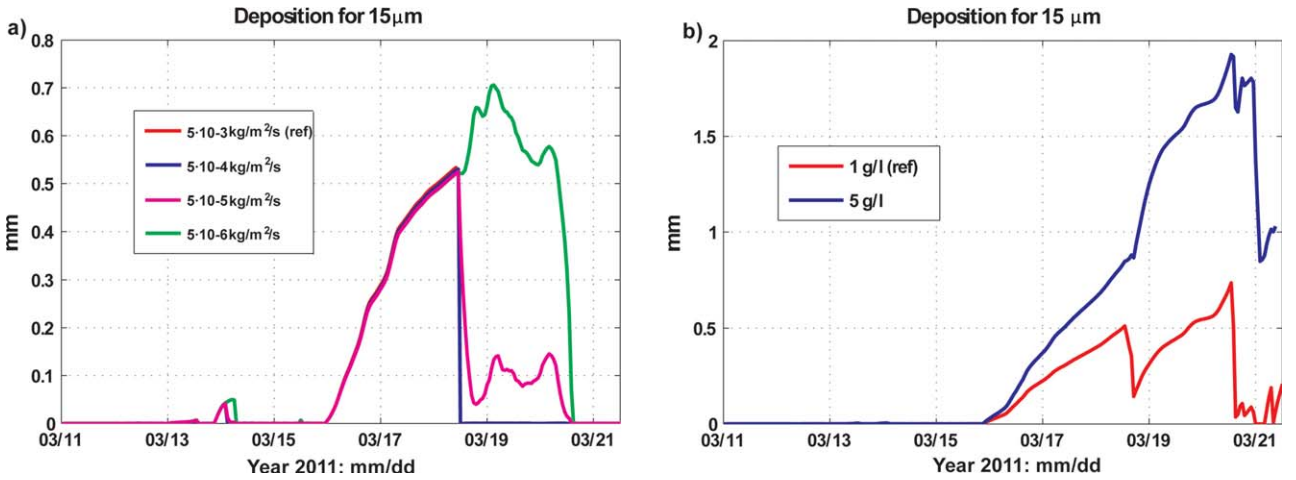

Figure 9. Time series of the deposition rates of the sensitivity tests for the sediment class 15 μm. (a) Deposition rates at 10 m water depth (P1) for different erodibility constant values (E_0 in $kg \cdot m^{-2} \cdot s^{-1}$). Note that the blue line overlaps the red line. (b) Deposition rates at 30 m water depth (30 m) for different suspended sediment river yield: 1 and 5 $mg \cdot L^{-1}$. The reference simulation is marked in both plots in red. Note that the *y* axis value varies in both subplots. Dates in *x* axis represent month/day.

caused by the settling of sediment resuspended at shallower than 10 m areas with the 21 March event eroding all the accumulated material.

Although varying erosion rates resulted in distinct depositional behaviors, all cases agreed in the preferential depositional areas and the subsequent reworking due to wave action. To better estimate the deposit area of the Besòs River, additional and extensive field observations of the accumulation process and a better estimation of the sediment yield of Besòs River would be desirable.

The sediment yield from the Besòs River used in the simulations is estimated from highly variable observations near its mouth [*Liquete et al*., 2009]. When compared with fluvial delivery models, *Liquete et al*. [2009] noted that the observed sediment yield was probably underestimated during extreme events due to the typical torrential regime and the low frequency of measurements. To address the potential increase in sediment discharge, an additional simulation was conducted with a sediment yield of 5 $g \cdot L^{-1}$. In this simulation, the deposition pattern exhibited a similar behavior in shape to the reference one, but the accumulation rate differed significantly. Accumulations on the order of a few mm were obtained for a sediment yield of 5 $g \cdot L^{-1}$ (Figure 9b). Furthermore, the reworking due to wave action was also observed at 30 m being similar to the reference simulation. The effect of the enhanced discharge was an increase in deposit thickness, but the timing and magnitude of the process were not considerably altered.

A more complex behavior is expected because of spatially variable critical stresses, porosity, and erosion rates. Other physical-chemical effects typical of cohesive sediments [*Van Ledden et al*., 2004; *Winterwerp and van Kesteren*, 2004] will alter the linearity of the erosion fluxes presented in equation (1) [*Sanford and Maa*, 2001]. However, the behavior shown for the modeled cases could be extrapolated to accumulation and erosion sequences with sediment availability limiting the erosion depending on the intensity of the storm. Additional experiments that include cohesive bed behavior, more than two grain-size classes, considering physical-chemical factors, or taking into account flocculation effects in the settling fluxes will be needed to understand the importance of these processes in the mud deposits formation.

4.2. Cross-Shelf Sediment Fluxes

Net sediment transport across the shelf is difficult to estimate due to the mechanisms involved [*Nittrouer and Wright*, 1994]. In the inner and midshelf (less than 100 m bottom depth), seaward fluxes may respond to a complex combination of wave-driven undertow that extends offshore of the surf zone [*Lentz et al*., 2008], Ekman transport during downwelling-favorable winds [*Cudaback et al*., 2005], cross-shelf fluxes during relaxation periods after wind pulses [*Grifoll et al*., 2012], or divergences in the along-shelf flow that result in increased cross-shelf flow [*Kirincich and Barth*, 2009]. In shallower areas (less than 50 m bottom depth), the correlation between sediment flux pulses and wave energy suggested a final depositional area

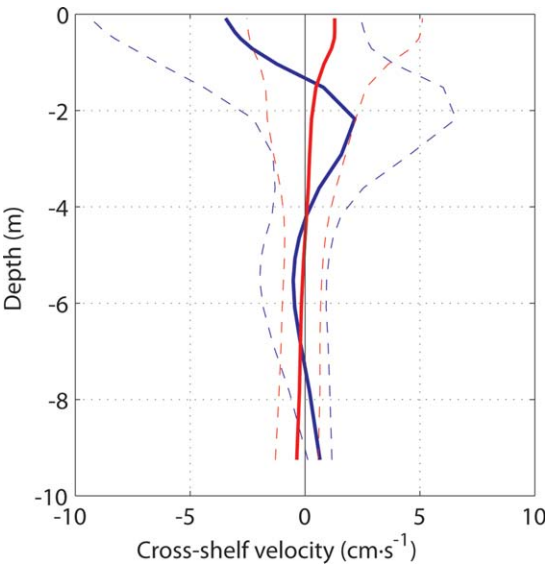

Figure 10. Vertical profiles of cross-shelf velocity at P1 (10 m) for an energetic period (blue) and during a calm period (red). Standard deviations are shown in dashed line. *x* Axis shows positive velocity offshore.

controlled by wave-driven flow. Averaged cross-shelf velocity profiles at 10 m (Figure 10) during the storm period of 15 March exhibited net offshore flow below the subsurface. The cross-shelf velocity during the calm period (16–18 March) exhibited smaller flows without evident relation to along-shelf fluxes. The influence of the wave-driven fluxes in the cross-shelf dynamics exemplified the wave-dominated nature of the shelf in NW Mediterranean Sea as suggested by several observational studies [*Jiménez et al*., 1999; *Puig et al*., 2001; *Palanques et al*., 2002; *Guillén et al*., 2006].

4.3. Short-Term Deposition

The modeled depositional pattern revealed the three initial dispersal stages suggested by *Wright and Nittrouer* [1995]. Stage I (initial river plume) was associated with periods of moderate near-bottom SSC without sediment accumulation on the bed (12–16 March). Stage II (initial deposition) was characterized by large accumulation at shallower areas than 30 m (see Figures 5a, 5b, 6i, and 6j), corresponding to the tail of the storm (16–18 March). Stage III was associated with resuspension and transport due to sediment availability in the bottom and enhanced bed stress. Stage III included the energetic period that started 18 March when erosion at 10 m was balanced by accumulation of fine sediment at 30 and 50 m. The wave peak during 20 March caused sediment resuspension and transport and removed the previous fine deposit from the ephemeral layers.

The evolution of ephemeral sedimentary deposits after a flood and the subsequent reworking due to wave action identified in the Besòs River system can explain the observed fine deposits. The modeled preferential flash flood deposit agreed with the observed spatial distribution of fines in the vicinity of the Besòs mouth. This was consistent with the description of *Wright and Nittrouer* [1995] for small mountainous rivers characterized by relatively rapid deposition near the mouth [*Bever et al*., 2011]. For instance, *Guillén et al*. [2006] found observational evidence of sediment deposition near the mouth of the Tet River. The initial sediment layer observed near the Tet River mouth corresponded to an ephemeral layer on the inner-shelf deposited during the tail of the flood. This deposit was later resuspended, transported offshore, and deposited in the midshelf a few days after by a subsequent storm with energetic wave action in a similar manner to the presented Besòs River material. The short temporal scale of the freshwater discharge, the effect of the wave-induced currents, and the wind enhanced mixing of the buoyant plume promoted rapid initial deposition close to the Besòs River mouth (Figures 6i and 6j). A similar behavior has been described for sediment from the Waipoa River (New Zealand) affected by oceanic storms; the sediment delivery coincided with energetic wave and current conditions the near-shore initial sediment deposition area subsequently got reworked by wave action and transported offshore [*Bever et al*., 2011].

Retention periods of ephemeral inner-shelf deposits have been estimated in several observational studies. Different temporal scales were found from observed inner-shelf deposits ranging from 4 days on the Eel River shelf [*Traykovski et al*., 2000], to a few weeks in Poverty Bay [*Bever and Harris*, 2013] and 2 months in the Tet River system [*Guillèn et al*., 2006]. In our case, reworking and transport offshore from the shallowest area (10 m) after the flood event (Figures 6i and 6j) occurred under relatively weak wave conditions (0.7 m significant wave height at the beginning of the energetic period of 18 March). The significant wave height peak during the energetic event (18 March) showed a complete reworking of the material deposited at

Table 3. Number of Wave Episodes that Exceeded Significant Wave Height of 1 and 1.5 m During the May 2010 to April 2011 Period

	Spring	Summer	Fall	Winter	Total
Hs > 1 m	16	8	42	17	83
Hs > 1.5 m	7	1	11	13	32

30 m water depth (Figures 6i and 6j). Thus, subsequent sediment resuspension depends on the period between energetic wave events and the river sediment availability. It is illustrative that relatively low-energy conditions were able to resuspend recently deposited sediment.

The final modeled deposit from the Besòs River diverged from the expected river plume route. The Besòs River plume tends to be attached to the coast and highly influenced by the local winds [*Liste et al*., 2014]. This behavior was induced by settling fluxes that prevailed against the buoyant flow in the case of relatively low discharge where the plume remained detached from the bottom [*Geyer et al*., 2004]. Observations of the buoyant plume [*Grifoll et al*., 2012] confirmed that the pycnocline was observed far from the bottom during enhanced river discharge conditions.

4.4. Long-Term Implications

Guillèn et al. [2006] noted that sediment across the shelf follows a complex, multistep pattern that needs to be studied using a multievent approach. In our study, this approach was carried out using different time scales to evaluate the initial dispersal, subsequent reworking and final mud belt configuration. The depositional pattern produced by a short-term model simulation in March 2011 partially mimics aspects of the long-term depositional pattern. The final configuration of the river deposits responds to shelf hydrodynamics in temporal scales larger than a few days [*Harris et al*., 2008; *Bever et al*., 2009; *Xu et al*., 2011]. The 1 year simulation allowed the explanation of the final mud deposit configuration and a comparison with the observed grain-size distribution.

The results of the 1 year simulation suggested the shifted depocenter of the mud deposit and the coarser gradation in the southern part of the domain as seen in observations. The long-term-averaged flow [*Grifoll et al*., 2013b] resulted in a south-westward drift. The 5% exceedance metric provided a clear limit of the fine deposits. The flow convergence, from the narrowing of the continental shelf, and the resulting intensification south of the Besòs River determined the grain-size gradation of the seabed. Modeled bed mobility confirmed the preferential mud deposition region was surrounded by an energetic current-induced bottom stress region (caused by flow convergence) to the south, a region of enhanced flow near the shelf break (offshore edge), and an enhanced wave-induced bottom stress region (onshore edge). The bed mobility for areas shallower than 30 m bottom depth was dominated by the wave action as suggested in previous studies of the NW Mediterranean Sea [*Jiménez et al*., 1999; *Puig et al*., 2001; *Palanques et al*., 2002; *Guillèn et al*., 2006].

The material accumulated during flash flood events and its remobilization depends on the occurrence of two distinct storm types: (a) "wet" storms that increase sediment availability on the shelf through increased river discharge; and (b) "dry" storms that are characterized by energetic wave conditions but no precipitation [*Guillén et al*., 2006]. The 14–16 March event represented a "wet" storm, while the 18–20 March event was an example of "dry" conditions. During spring-summer, the wave climate is less energetic (the bed mobility percentage was lower) but sediment availability in the form of ephemeral layers can be significant during spring. During winter and fall, the wave energy increases resulting in enhanced bed mobility. Additionally, river flow increases during fall [*Grifoll et al*., 2013b]. The enhanced fall-winter stress has the ability to mobilize not only the recently deposited material, but also the remaining material from the previous spring-summer period that was not resuspended from the ephemeral layers during low wave-energy conditions.

Based on the short-term analysis, we established that wave episodes that exceed 1 m significant wave height were able to remobilize deposited sediment at depths less than 10 m; and wave episodes that exceeded 1.5 m were able to erode sediment at 30 m (Figure 6). Table 3 presents the number of episodes that the wave conditions were exceeded for 1 year model simulation period (May 2010 to April 2011). Of the 83 episodes that exceeded 1 m significant wave height, one half occurred during fall and one fifth during both spring and winter. The episodes that exceeded 1.5 m occurred predominantly in fall and winter. Energetic wave events were less likely in summer. Thus, considering that wave action is the main process controlling resuspension and that the currents followed a similar seasonal pattern [*Grifoll et al*., 2013a, 2013b], remobilization also exhibited a strong seasonal modulation limited by sediment availability (most

material from the ephemeral layers was likely eroded by fall storms, so winter events might have a limited remobilization effect). Thus, a seasonal pattern in the fine sediment formation is expected based on sediment availability and the number, strength and character (wet versus dry) of storms.

Liquete et al. [2007] hypothesized on the role of shelf flow in generating the south-westward sediment drift and on the final deposit configuration. We demonstrate that most of the shelf transport and deposition seems limited to a few km near the Besòs River mouth and that the initial deposition occurs relatively fast compared to larger systems [*Wright and Nittrouer*, 1995]. *Guillèn et al*. [2006] noted that the rivers in the NW Mediterranean Sea cannot be understood as isolated systems as there is interaction between different river sediment contributions. For instance, the Llobregat River (located south of Barcelona Harbor) could play a role on the sediment dispersal or the amount of sediment exported to the outer shelf and slope area. *Checa et al*. [1986] noted that the prodeltaic Besòs and Llobregat rivers converge and cannot be differentiated based on seismic cartography. To address these interconnections, additional water and sediment flux observations and altimetry measurements would be desirable, in particular from the southern margin of the shelf in front of Barcelona.

5. Concluding Remarks

In this contribution, we have analyzed the formation process of fine deposits resulting from flash flood events in the Besòs River (NW Mediterranean Sea). The use of the COAWST modeling system has proven to be a useful tool to investigate the mechanisms controlling the formation of the observed fine sediment deposits. The numerical results of this high-resolution model show preferential sediment deposition as a result of river discharge and subsequent reworking due to wave action. The model indicates wave-induced seaward fluxes are the mechanism responsible for the formation of fine deposits over short-time scales. Additionally, the final fine deposit shape responded to long-term flow over the shelf dominated by a south-westward net flow and flow convergence in front of Barcelona Harbor. According to the short and long-term analyses a seasonal pattern in the fine deposit formation is expected. This study provides a plausible interpretation of mud belt formation due to sediment yield from flash flood rivers in a microtidal regime.

Acknowledgments

The author wants to acknowledge the helpful comments and suggestions from Pat Dickhudt (USGS, Woods Hole), P. Soupy Dalyander (USGS, St. Petersburg), and Jose Jiménez and Juan Fernandez (LIM/UPC Laboratory of Marine Engineering, Technical University of Catalonia, Barcelona). The authors are thankful to Joan Puigdefàbregas (LIM/UPC, Barcelona) and Jordi Cateura (LIM/UPC, Barcelona) for the data acquisition. The research leading to these results and data acquisition has received funding from the Field_ac (FP7/2007/2013-242284), Mestral (CTM-2011-30489), and ICOAST project (ECHO/SUB/2013/661009). We acknowledge XIOM network (www.lim.cat) and ACA Water Catalan Agency (www.gencat.cat/aca) for the data provided.

References

Alomar, M., A. Sánchez-Arcilla, R. Bolaños, and A. Sairouni (2014), Wave growth and forecasting in variable, semi-enclosed domain, *Cont. Shelf Res.*, doi:10.1016/j.csr.2014.05.008, in press.

Amoudry, L. O., and A. J. Souza (2011), Deterministic coastal morphological and sediment transport modeling: a review and discussion, *Rev. Geophys.*, *49*, RG2002, doi:10.1029/2010RG000341.

Ariathurai, C. R., and K. Arulanandan (1978), Erosion rates of cohesive soils, *J. Hydraul. Div. Am. Soc. Civ. Eng.*, *104*(2), 279–282.

Bever, A. J., and C. K. Harris (2013), Storm and fair-weather driven sediment-transport within Poverty Bay, New Zealand, evaluated using coupled numerical models, *Cont. Shelf Res.*, doi:10.1016/j.csr.2013.07.012.

Bever, A. J., C. K. Harris, C. R. Sherwood, and R. P. Signell (2009), Deposition and flux of sediment from the Po River, Italy: An idealized and wintertime numerical modeling study, *Mar. Geol.*, *260*(1–4), 69–80, doi:10.1016/j.margeo.2009.01.007.

Bever, A. J., J. E. McNinch, and C. K. Harris (2011), Hydrodynamics and sediment-transport in the nearshore of Poverty Bay, New Zealand: Observations of nearshore sediment segregation and oceanic storms, *Cont. Shelf Res.*, *31*(6), 507–526, doi:10.1016/j.csr.2010.12.007.

Bolaños, R., G. Jorda, J. Cateura, J. Lopez, J. Puigdefabregas, J. Gomez, and M. Espino (2009), The XIOM: 20 years of a regional coastal observatory in the Spanish Catalan coast, *J. Mar. Syst.*, *77*(3), 237–260, doi:10.1016/j.jmarsys.2007.12.018.

Booij, N., R. C. Ris, and L. H. Holthuijsen (1999), A third-generation wave model for coastal regions 1. Model description and validation, *J. Geophys. Res.*, *104*(C4), 7649–7666, doi:10.1029/98JC02622.

Bourrin, F., P. L. Friend, C. L. Amos, E. Manca, C. Ulses, A. Palanques, X. D. de Madron, and C. E. L. Thompson (2008), Sediment dispersal from a typical Mediterranean flood: The Têt River, Gulf of Lion, *Cont. Shelf Res.*, *28*, 1895–1910, doi:10.1016/j.csr.2008.06.005.

Cudaback, C. N., L. Washburn, and E. Dever (2005), Subtidal inner-shelf circulation near Point Conception, California, *J. Geophys. Res.*, *110*, C10007, doi:10.1029/2004JC002608.

Dalyander, P. S., B. Butman, C. R. Sherwood, R. P. Signell, and J. L. Wilkin (2013), Characterizing wave- and current-induced bottom shear stress: U.S. middle Atlantic continental shelf, *Cont. Shelf Res.*, *52*, 73–86, doi:10.1016/j.csr.2012.10.012.

Díaz, J., A. Palanques, C. H. Nelson, and J. Guillén (1996), Morpho-structure and sedimentology of the Holocene Ebro prodelta mud belt (northwestern Mediterranean Sea), *Cont. Shelf Res.*, *16*(4), 435–456, doi:10.1016/0278-4343(95)00019-4.

Dickhudt, P. J., C. T. Friedrichs, and L. P. Sanford (2011), Mud matrix solids fraction and bed erodibility in the York River estuary, USA, and other muddy environments, *Cont. Shelf Res.*, *31*(10), S3–S13, doi:10.1016/j.csr.2010.02.008.

Dufois, F., R. Verney, P. Le Hir, F. Dumas, and S. Charmasson (2014), Impact of winter storms on sediment erosion in the Rhone River prodelta and fate of sediment in the Gulf of Lions (North Western Mediterranean Sea), *Cont. Shelf Res.*, *72*, 57–72, doi:10.1016/j.csr.2013.11.004.

Fan, S., D. J. P. Swift, P. Traykovski, S. Bentley, J. C. Borgeld, C. W. Reed, and A. W. Niedoroda (2004), River flooding, storm resuspension, and event stratigraphy on the northern California shelf: Observations compared with simulations, *Mar. Geol.*, *210*(1–4), 17–41, doi:10.1016/j.margeo.2004.05.024.

Ferré, B., K. Guizien, X. D. de Madron, A. Palanques, J. Guillén, and A. Grémare (2005), Fine-grained sediment dynamics during a strong storm event in the inner-shelf of the Gulf of Lion (NW Mediterranean), *Cont. Shelf Res.*, *25*(19–20), 2410–2427, doi:10.1016/j.csr.2005.08.017.

Fox, J. M., P. S. Hill, T. G. Milligan, and A. Boldrin (2004), Flocculation and sedimentation on the Po River Delta, *Mar. Geol.*, *203*(1–2), 95–107, doi:10.1016/S0025–3227(03)00332-3.

George, A. D., and P. S. Hill (2008), Wave-climate, sediment supply and the depth of the sand-mud transition: A global survey, *Mar. Geol.*, *254*, 121–128, doi:10.1016/j.margeo.2008.05.005.

Geyer, W. R., P. S. Hill, and G. C. Kineke (2004), The transport, transformation and dispersal of sediment by buoyant coastal flows, *Cont. Shelf Res.*, *24*(7–8), 927–949, doi:10.1016/j.csr.2004.02.006.

Grifoll, M., A. L. Aretxabaleta, M. Espino, and J. C. Warner (2012), Along-shelf current variability on the Catalan inner-shelf (NW Mediterranean), *J. Geophys. Res.*, *117*, 1–14, doi:10.1029/2012JC008182.

Grifoll, M., V. Gracia, J. Fernandez, and M. Espino (2013a), Suspended sediment observations in the Barcelona inner-shelf during storms, in *Proceedings 12th International Coastal Symposium*, edited by D. C. Conley et al., vol. 1, pp. 1533–1538, Plymouth, England, U. K.

Grifoll, M., A. L. Aretxabaleta, J. L. Pelegrí, M. Espino, J. C. Warner, and A. Sánchez-Arcilla (2013b), Seasonal circulation over the Catalan inner-shelf (northwest Mediterranean Sea), *J. Geophys. Res. Ocean*, *118*, 5844–5857, doi:10.1002/jgrc.20403.

Guillén, J., F. Bourrin, A. Palanques, X. D. de Madron, P. Puig, and R. Buscail (2006), Sediment dynamics during wet and dry storm events on the Têt inner shelf (SW Gulf of Lions), *Mar. Geol.*, *234*(1–4), 129–142, doi:10.1016/j.margeo.2006.09.018.

Harris, C. K., C. R. Sherwood, R. P. Signell, A. J. Bever, and J. C. Warner (2008), Sediment dispersal in the northwestern Adriatic Sea, *J. Geophys. Res.*, *113*, C11S03, doi:10.1029/2006JC003868.

Jiménez, J. A., J. Guillén, V. Gracia, A. Palanques, M. A. García, A. Sánchez-Arcilla, P. Puig, J. Puigdefábregas, and G. Rodríguez (1999), Water and sediment fluxes on the Ebro Delta shoreface: On the role of low frequency currents, *Mar. Geol.*, *157*(3–4), 219–239, doi:10.1016/S0025-3227(98)00153-4.

Kirincich, A. R., and J. A. Barth (2009), Alongshelf variability of inner-shelf circulation along the Central Oregon Coast during summer, *J. Phys. Oceanogr.*, *39*(6), 1380–1398, doi:10.1175/2008JPO3760.1.

Kumar, N., G. Voulgaris, J. C. Warner, and M. Olabarietta (2012), Implementation of the vortex force formalism in the Coupled Ocean-Atmosphere-Wave-Sediment Transport (COAWST) modeling system for inner shelf and surf zone applications, *Ocean Model.*, *47*, pp. 65–95.

Lentz, S. J., M. Fewings, P. Howd, J. Fredericks, and K. Hathaway (2008), Observations and a model of undertow over the inner continental shelf, *J. Phys. Oceanogr.*, *38*(11), 2341–2357, doi:10.1175/2008JPO3986.1.

Liquete, C., M. Canals, G. Lastras, D. Amblas, R. Urgeles, B. De Mol, M. De Batist, and J. E. Hughes-Clarke (2007), Long-term development and current status of the Barcelona continental shelf: A source-to-sink approach, *Cont. Shelf Res.*, *27*(13), 1779–1800, doi:10.1016/j.csr.2007.02.007.

Liquete, C., M. Canals, W. Ludwig, and P. Arnau (2009), Sediment discharge of the rivers of Catalonia, NE Spain, and the influence of human impacts, *J. Hydrol.*, *366*(1–4), 76–88, doi:10.1016/j.jhydrol.2008.12.013.

Liste, M., M. Grifoll, and J. Monbaliu (2014), River plume dispersion in response to flash-flood events. Application to the Catalan shelf, *Cont. Shelf Res.*, doi:10.1016/j.csr.2014.06.007.

Madsen, O. S. (1994), Spectral wave-current bottom boundary layer flows, in *Proceedings of the 24th International Conference on Coastal Engineering*, vol. 1, pp. 384–398, Am. Soc. of Civ. Eng., Kobe, Japan.

Madsen, O. S., L. D. Wright, J. D. Boon, and T. A. Chisholm (1993), Wind stress, bed roughness and sediment suspension on the inner shelf during an extreme storm event, *Cont. Shelf Res.*, *13*(11), 1303–1324, doi:10.1016/0278-4343(93)90054-2.

McCave, I. N. (1972), Transport and escape of fine-grained sediment from shelf seas, in *Shelf Sediment Transport: Process and Pattern*, edited by D. J. P. Swift, D. B. Duane, and O. H. Pilkey, pp. 225–248, Dowden Hutchinson Ross, Stroudsburg, Pa.

Nittrouer, C. A., and L. D. Wright (1994), Transport of particles across continental helves, *Rev. Geophys.*, *32*(1), 85–113.

Ogston, A., and R. Sternberg (1999), Sediment-transport events on the northern California continental shelf, *Mar. Geol.*, *154*(1–4), 69–82, doi:10.1016/S0025–3227(98)00104-2.

Ogston, A., D. Cacchione, R. Sternberg, and G. Kineke (2000), Observations of storm and river flood-driven sediment transport on the northern California continental shelf, *Cont. Shelf Res.*, *20*(16), 2141–2162, doi:10.1016/S0278-4343(00)00065-0.

Palanques, A., P. Puig, J. Guillén, J. Jiménez, V. Gracia, A. Sánchez-Arcilla, and O. Madsen (2002), Near-bottom suspended sediment fluxes on the microtidal low-energy Ebro continental shelf (NW Mediterranean), *Cont. Shelf Res.*, *22*(2), 285–303, doi:10.1016/S0278–4343(01)00058-9.

Palanques, A., P. Puig, J. Guillén, M. Demestre, and J. Martín (2014), Effects of bottom trawling on the Ebro continental shelf sedimentary system (NW Mediterranean), *Cont. Shelf Res.*, *72*, 83–98, doi:10.1016/j.csr.2013.10.008.

Pallares, E., A. Sánchez-Arcilla, and M. Espino (2014), Wave energy balance in wave models (SWAN) for semi-enclosed domains—Application to Catalan coast, *Cont. Shelf Res.*, doi:10.1016/j.csr.2014.03.008.

Puig, P., A. Palanques, and J. Guillén (2001), Near-bottom suspended sediment variability caused by storms and near-inertial internal waves on the Ebro mid continental shelf (NW Mediterranean), *Mar. Geol.*, *178*(1–4), 81–93, doi:10.1016/S0025-3227(01)00186-4.

Rodi, W. (1987), Examples of calculation methods for flow and mixing in stratified fluids, *J. Geophys. Res.*, *92*(C5), 5305–5328.

Rovira, A., and R. J. Batalla (2006), Temporal distribution of suspended sediment transport in a Mediterranean basin: The Lower Tordera (NE SPAIN), *Geomorphology*, *79*(1–2), 58–71, doi:10.1016/j.geomorph.2005.09.016.

Sanford, L. P., and J. P.Y. Maa (2001), A unified erosion formulation for fine sediments, *Mar. Geol.*, *179*, 9–23.

Shchepetkin, A. F., and J. C. McWilliams (2005), The regional oceanic modeling system (ROMS): A split-explicit, free-surface, topography-following-coordinate oceanic model, *Ocean Modell.*, *9*(4), 347–404.

Sherwood, C. R., B. Butman, D. A. Cacchione, D. E. Drake, T. F. Gross, R. W. Sternberg, P. L. Wiberg, and A. J. Williams (1994), Sediment-transport events on the northern California continental shelf during the 1990–1991 STRESS experiment, *Cont. Shelf Res.*, *14*(10–11), 1063–1099, doi:10.1016/0278-4343(94)90029-9.

Soulsby, R. (1997), *Dynamics of Marine Sands: A Manual for Practical Applications*, pp. 97–110, Thomas Telford, London, U. K.

Tonani, M., N. Pinardi, C. Fratianni, J. Pistoia, S. Dobricic, S. Pensieri, M. de Alfonso, and K. Nittis (2009), Mediterranean forecasting system: Forecast and analysis assessment through skill scores, *Ocean Sci.*, *5*(4), 649–660.

Traykovski, P., W. R. Geyer, J. Irish, and J. Lynch (2000), The role of wave-induced density-driven fluid mud flows for cross-shelf transport on the Eel River continental shelf, *Cont. Shelf Res.*, *20*(16), 2113–2140, doi:10.1016/S0278-4343(00)00071-6.

Ulses, C., C. Estournel, X. D. de Madron, and A. Palanques (2008), Suspended sediment transport in the Gulf of Lions (NW Mediterranean): Impact of extreme storms and floods, *Cont. Shelf Res.*, *28*(15), 2048–2070, doi:10.1016/j.csr.2008.01.015.

Umlauf, L., and H. Burchard (2003), A generic length-scale equation for geophysical turbulence models, *J. Mar. Res.*, *61*, 235–265.
Van Ledden, M., W. G. van Kesteren, and J. Winterwerp (2004), A conceptual framework for the erosion behaviour of sand–mud mixtures, *Cont. Shelf Res.*, *24*(1), 1–11, doi:10.1016/j.csr.2003.09.002.
Vousdoukas, M. I., R. Verney, F. Dufois, C. Pinazo, D. Sauzade, S. Meule, P. Cann, and T. A. Plomaritis (2011), Sediment dynamics in the Bay of Marseille, Gulf of Lions (France): Hydrodynamic forcing vs. bed erodibility, *J. Coastal Res.*, *27*(5), 942–958, doi:10.2112/JCOASTRES-D-10-00122.1.
Warner, J. C., C. R. Sherwood, H. G. Arango, and R. P. Signell (2005), Performance of four turbulence closure models implemented using a generic length scale method, *Ocean Modell.*, *8*(1–2), 81–113, doi:10.1016/j.ocemod.2003.12.003.
Warner, J. C., B. Butman, and P. S. Dalyander (2008a), Storm-driven sediment transport in Massachusetts Bay, *Cont. Shelf Res.*, *28*(2), 257–282, doi:10.1016/j.csr.2007.08.008.
Warner, J. C., C. Sherwood, R. P. Signell, C. K. Harris, and H. G. Arango (2008b), Development of a three-dimensional, regional, coupled wave, current, and sediment-transport model, *Comput. Geosci.*, *34*, 1284–1306.
Warner, J. C., B. Armstrong, R. He, and J. B. Zambon (2010), Development of a coupled ocean–atmosphere–wave–sediment transport (COAWST) modeling system, *Ocean Modell.*, *35*(3), 230–244, doi:10.1016/j.ocemod.2010.07.010.
Widdows, J., M. D. Brinsley, and N. D. Pope (2009), Effect of Nereis diversicolor density on the erodibility of estuarine sediment, *Mar. Ecol. Prog. Ser.*, *378*, 135–143.
Winterwerp, J. C., and W. G. M. van Kesteren (2004), Introduction to the Physics of Cohesive Sediment in the Marine Environment, Dev. Sedimentol., vol. 56, pp. 386–396, Elsevier, Amsterdam.
Wright, L. D., and C. A. Nittrouer (1995), Dispersal of river sediments in coastal seas: Six contrasting cases, *Estuaries*, *18*(3), 494–508, doi:10.2307/1352367.
Xu, K., C. K. Harris, R. D. Hetland, and J. M. Kaihatu (2011), Dispersal of Mississippi and Atchafalaya sediment on the Texas–Louisiana shelf: Model estimates for the year 1993, *Cont. Shelf Res.*, *31*(15), 1558–1575, doi:10.1016/j.csr.2011.05.008.
Xue, Z., R. He, J. P. Liu, and J. C. Warner (2012), Modeling transport and deposition of the Mekong River sediment, *Cont. Shelf Res.*, *37*(1), 66–78, doi:10.1016/j.csr.2012.02.010.